Hindawi
Journal of Nanomaterials
Volume 2019, Article ID 5198045, 16 pages
https://doi.org/10.1155/2019/5198045

Research Article

Synthesis of Porous Octahedral ZnO/CuO Composites from Zn/Cu-Based MOF-199 and Their Applications in Visible-Light-Driven Photocatalytic Degradation of Dyes

Tran Thanh Minh,[1] Nguyen Thi Thanh Tu,[2] Tran Thi Van Thi,[1] Le Thi Hoa,[1] Hoang Thai Long,[1] Nguyen Hai Phong,[1] Thong Le Minh Pham,[3] and Dinh Quang Khieu[1]

[1]*University of Sciences, Hue University, 530000, Vietnam*
[2]*Institute for Environmental Science, Nguyen Tat Thanh University, 700000, Vietnam*
[3]*Institute of Research and Development, Duy Tan University, 550000, Vietnam*

Correspondence should be addressed to Dinh Quang Khieu; dqkhieu@hueuni.edu.vn

Received 22 June 2019; Revised 4 September 2019; Accepted 16 September 2019; Published 14 October 2019

Academic Editor: Sesha Srinivasan

In the present paper, a porous octahedral (ZnO/CuO) composite is synthesized from zinc/copper-based metal-organic framework-199, and its applications in visible-light-driven photocatalytic degradation of dyes are demonstrated. The precursors of Zn-BTC, Cu-BTC, and Zn/Cu-BTC (BTC: benzene-1,3,5-tricarboxylate) were synthesized using a microwave-assisted method. Benzene-1,3,5-tricarboxylate acts as a sacrificial template and was removed from the precursors via thermal decomposition to form CuO, ZnO, and ZnO/CuO. ZnO/CuO with a large specific surface area of 32.5 $m^2 \cdot g^{-1}$ is composed of porous octahedral particles of 5–10 μm in diameter. Methylene blue (MB) was utilized as the dye model for photocatalytic degradation reactions. The porous octahedral ZnO/CuO exhibits superior visible-light-driven photocatalytic degradation of MB compared with single CuO or ZnO. The kinetic model of photocatalytic degradation was proposed as $(1/K_L) \times \ln C + C = -k_r t + (1/K_L) \times \ln C_e + C_e$, where K_L is the Langmuir equilibrium constant and C_e is the MB concentration at equilibrium. The model significantly fits the kinetic data. In addition, the acquired catalyst manifests excellent photocatalytic degradation for several other dyes including phenol red, methyl orange, and Congo red.

1. Introduction

Metal oxide semiconductors are widely used for photocatalytic degradation of organic pollutants due to their high photosensitivity, nontoxic nature, and low cost. It is well known that titanium oxide (TiO_2) and zinc oxide (ZnO) can only be excited for photocatalysis. ZnO belongs to the *n*-type semiconductor and is considered one of the important semiconductor photocatalysts due to its high photosensitivity and stability [1, 2]. However, the constraint of ZnO among others is that it absorbs light only in the near UV region because of its large bandwidth of 3.2 eV. Unfortunately, sunlight constitutes only 4–5% of UV light [3, 4]. Therefore, the effective use of solar energy still remains a challenge in photocatalytic application. The photoresponse of narrow-band-gap semiconductors shifts much more to the visible wavelength range. However, these semiconductors are difficult to maintain their photoactivity for a long time due to the recombination of the photo-induced electron-hole pairs. To improve the visible-light-driven photocatalytic efficiency of ZnO, some metals or oxides are often introduced to its surface. Au-loaded ZnO can significantly enhance the activities of photogenerated electrons by suppressing the recombination of charge carriers [5]. Unlike pure ZnO, mesoporous Fe_2O_3/ZnO core-shell composites manifest an excellent photocatalytic degradation of Rhodamine B in both ultraviolet and visible light regions [6]. The nanostructure of cupric oxide (CuO) is the *p*-type semiconductor with a narrow band gap of 1.2–2.71 eV. Despite its high capacity of absorption in the visible light range, CuO is surprisingly not appealing in terms of catalytic behavior due to its fast recombination rate of the induced electron-hole pairs. Thus, in order to

achieve a high catalytic activity, a synergistic system may be expected by connecting CuO with ZnO, in which CuO acts as a cocatalyst and thus expands the visible-light response. Moreover, the possible formation of favorable *p-n* junctions at the nanostructure interface restrains the photo-induced carrier recombination. Various approaches have been accomplished to synthesize ZnO/CuO composites for photocatalytic application such as sol-gel and coprecipitation [7–9]. However, to achieve a high degree of homogeneous dispersion of each component still remains a major challenge with multimetal oxides.

Metal-organic frameworks (MOFs) are a class of crystalline materials that have coordination bonds between transition-metal cations and organic ligands. The metal-organic frameworks possess unique performance advantages, such as controllable pore size and pore surface, low density, and large surface area. These outstanding properties make MOFs widely used in many fields, for example, adsorption, photocatalysis, and biosensors [10–12]. HKUST-1 (Hong Kong University of Science and Technology) is one of the first MOFs made up of copper nodes with benzene-1,3,5-tricarboxylic (BTC) acid struts between them [13]. HKUST-1 (or MOF-199 or Cu-BTC) manifests remarkable potentials in photocatalysis [14, 15] and separation [16]. MOF-199 notably displays persistence in both water and air [13]. Zinc is a promising metal that constructs an isostructural analogue to Cu-BTC. Anbia et al. [17] reported the hydrothermal synthesis of Zn-BTC that can be a good material for hydrogen storage at room temperature. Zn-BTC is also synthesized through direct precipitation in solution under ultrasonic condition [18]. Xu et al. [19] reported the ionothermal synthesis of Zn-BTC using 1-ethyl-3-methylimidazolium bromide ionic liquid as a solvent. The use of ionic liquid in the synthesis of Zn-BTC has shown a vast range of possibilities of controlling the structures and obtaining new materials by tuning the properties of the ionic liquid. Zn-BTC possesses lower-than-expected surface areas (a few meters to a few dozen meters), or it completely collapses upon the removal of guest molecules [20]. Generally, synthetic conditions (temperature, atmosphere, and posttreatment) are critical to the formation of MOF diffractions as well as their physicochemical properties [17, 18, 21].

Multimetal component MOFs have widely been synthesized by simultaneously mixing several metal species with organic ligands [22, 23]. There exist several advantages of using multimetal-component MOFs as sacrificial templates compared with other conventional templates [24]. They are as follows:

(i) The metal species in MOFs are mixed at molecular levels

(ii) Homogeneous morphologies of MOFs are critical regarding the preparation of anisotropic multimetal oxides that are difficult to fabricate using classical methods

(iii) Undesired aggregation or structural collapse of the framework during thermolysis can be minimized due to their structural strength

Xu et al. successfully synthesized hierarchical porous $ZnO/ZnCo_2O_4$ using one-step thermal calcining the as-prepared Zn-Co-MOF precursor [25]. Huang et al. reported hierarchical $NiFe_2O_4/Fe_2O_3$ nanotubes prepared from MOFs for superior lithium-ion batteries [26]. Wu et al. developed a facile method for the synthesis of a hybrid $Zn_xCo_{(3-x)}O_4$ composite via the thermal oxidative decomposition of bimetallic (Zn/Co) zeolitic imidazolate frameworks (ZIFs) [27]. Recently, Lei et al. demonstrated the hollow CuO/ZnO materials derived from zeolite imidazole framework-8. This material is a very promising photocatalyst for tetracycline degradation [28]. However, so far, little work has been carried out to prepare ZnO/CuO from MOFs.

In the present paper, a porous octahedral (ZnO/CuO) composite is synthesized from zinc/copper-based metal-organic framework-199, and its applications in visible-light-driven photocatalytic degradation of dyes are demonstrated. The precursors of Zn-BTC, Cu-BTC, and Zn/Cu-BTC are synthesized with a microwave-assisted method. In addition, pure Zn-BTC and Cu-BTC are prepared for the sake of comparison. Benzene-1,3,5-tricarboxylic acts as a sacrificial template and is removed by calcination. The kinetic model of photocatalytic degradation is proposed by combining the heterogeneous catalysis for unimolecular reactions with adsorption isotherms.

2. Experimental

2.1. Materials. Benzene-1,3,5-tricarboxylic acid ($C_6H_3(COOH)_3$, ≥95%) (denoted as BTC), copper nitrate trihydrate ($Cu(NO_3)_2{\cdot}3H_2O$, 99.5%), zinc nitrate tetrahydrate ($Zn(NO_3)_2{\cdot}4H_2O$, 98.5%), methyl orange ($C_{14}H_{14}N_3NaO_3S$, 85%), phenol red ($C_{19}H_{14}O_5S$, 90%), and Congo red ($C_{32}H_{22}N_6Na_2O_6S_2$, 85%), potassium iodide (KI, 99%), benzoquinone ($C_6H_4O_2$, 98%), and isopropanol (C_3H_7OH) were purchased from Merck, Germany. Dimethylformamide ($(CH_3)_2NCHO$), ethanol (C_2H_5OH), methanol (CH_3OH, 99% purity), and methylene blue ($C_{16}H_{18}ClN_3S$, 82%—MB) were acquired from HiMedia, India. Methylene blue is used as the dye model. Potassium iodide and benzoquinone are used as scavengers in the current study.

2.2. Apparatus. Powder X-ray diffraction patterns (PXRD) were performed on a D8 Advance Bruker monochromator equipped with a Cu-Kα radiation source ($\lambda = 1.5406$ Å). The morphologies of the obtained samples were analyzed using a scanning electron microscope (SEM) (Hitachi S-4800) and a high-resolution transmission electron microscope (HR-TEM) (JEM-2100). Thermo analysis (TG-DTA) was carried out using a TG-DTA instrument (DTG-60H Shimadzu) under atmospheric pressure at a heating rate of $10^{\circ}C{\cdot}min^{-1}$. Nitrogen adsorption/desorption isotherms were recorded on a Micromeritics ASAP 2020 instrument. The samples (200 mg) were degassed at 120°C for 24 h before measurements. The specific surface area was determined via the Brunauer-Emmett-Teller (BET) model with a relative pressure of 0.01–0.25 using adsorption data. Pore size distribution calculation was accomplished with the BJH (Barrett, Joyner, and Halenda) model using the adsorption branch of

the isotherms. The data of ultraviolet-visible diffuse reflectance spectroscopy (UV-Vis-DRS) were recorded on a Cary 5000 UV-Vis spectrometer (using $BaSO_4$ as the reference) at a collection speed of 600 nm·min^{-1}. X-ray photoelectron spectroscopy (XPS) was recorded with a Kratos Analytical spectrometer. All binding energies were referenced to the contaminant C 1s peak (at 284.6 eV) of adventitious carbon. The elemental compositions of Zn and Cu were analyzed with atomic absorption spectroscopy (AAS) using ZEEnit 7000. The elemental analysis of C and H was performed using Elemental Analyzer EA3000. Photoluminescence spectra of the obtained materials were measured at room temperature with a photoluminescence spectrophotometer (Horiba FL3). The concentration of dyes was measured using a UV-Vis spectrophotometer (V-630 Jasco) at λ_{max} 644 nm for methylene blue, 464 nm for methyl orange, 431 nm for phenol red, 500 nm for Congo red, and 270 nm for phenol. The degree of MB mineralization was calculated based on TOC (total organic carbon). The concentration of TOC was determined using a TOC analyzer (TOC-V_{CPH}).

2.3. Preparation of Zn/Cu-BTC, Cu-BTC, Zn-BTC, ZnO/CuO, CuO, and ZnO. Benzene-1,3,5-tricarboxylic acid (0.4410 g, 0.0021 mol), $Cu(NO_3)_2{\cdot}3H_2O$ (0.2289 g, 0.00095 mol), and $Zn(NO_3)_2{\cdot}4H_2O$ (0.5757 g, 0.0022 mol) were first dissolved in a mixture (21 mL) of ethanol, distilled water, and dimethylformamide (1 : 1 : 1 in *v*/*v*) and stirred magnetically for 5 min. The resultant mixture was then loaded into a 250 mL Erlenmeyer flask and placed in a hand-made microwave device (Sharp R-203VN-M with a power of 250 W) [29] and irradiated for 30 min. The solid was collected by centrifugation, washed with DMF three times, dried at 180°C for 8 h, and designated as Zn/Cu-BTC [29]. Zn-BTC and Cu-BTC were synthesized with the same procedure. Oxides (ZnO/CuO, ZnO, and CuO) were prepared by annealing Zn/Cu-BTC, Zn-BTC, and Cu-BTC at 500°C for 5 h at a heating rate of 5°C·min^{-1} under atmospheric pressure in an electric furnace (Vulcan 3-550 PD). The oxides were stored in a desiccator and used as a catalyst without any further treatment.

2.4. Photocatalytic Activity

2.4.1. Photocatalytic Performance. A beaker containing 500 mL of an aqueous suspension of MB (5–30 ppm) and 400 mg of catalyst was placed under a lamp bracket. The light source is a 160 W metal halide lamp (Philips) equipped with a wavelength cut-off filter ($\lambda \leq 420$ nm) (or Philips, Actinic BL 18 W, $\lambda = 365$ nm). Prior to illumination, the suspension was stirred magnetically in the dark for 60–180 min to ensure adsorption equilibrium. Three millilitres of the suspension was withdrawn at a certain time interval and centrifuged to remove the solid catalyst. The concentration of MB in the obtained clear liquid was analyzed using a UV-Vis spectrophotometer at $\lambda = 664$ nm. Further, the concentration of MB during illumination was determined using the aforesaid steps. In the scavenging test, potassium iodide, benzoquinone, and isopropanol were used as scavengers. A suspension of 100 mL MB (10 ppm) and 80 mg catalyst was first stirred in the dark, and 1 mL of the scavenger solution (2.4×10^{-2} M) was then added to the mixture under illumination.

2.4.2. Kinetic Analysis. The photocatalytic dye degradation kinetic is often investigated according to the *pseudo*-first-order kinetic model or the Langmuir-Hinshelwood model [30, 31] for heterogeneous catalysis as follows:

$$\ln \frac{C}{C_0} = -k \cdot t, \tag{1}$$

where C_0 and C are the initial concentration at time t (mg·L^{-1}) and k is the rate constant (min^{-1}).

However, the experimental design often involves two consecutive steps of dark adsorption and photocatalytic degradation. The problem to discuss here is the concentration C_0 in equation (1): whether it is the initial concentration or the equilibrium concentration just before illumination (C_e). Both of them seem unreasonable because C_e, in this case, is not an independent variable, but it depends on the balance of the dye in the solution and the adsorbent. C_0 is the initial concentration. However, as soon as the photocatalytic reaction occurs, the initial concentration is not C_0 but C_e. Most studies have ignored this issue. In order to overcome this obstacle, a new kinetic model is proposed by combining the heterogeneous catalysis for unimolecular reactions with the adsorption isotherms.

A heterogeneous catalyst first adsorbs the dye molecule from the aqueous solution onto its surface and then catalyzes the reaction under irradiation (two steps).

Step 1: adsorption

$$\text{Dye} + \text{surface} \longleftrightarrow \text{dye(adsorbed)(fast)} \tag{2}$$

Step 2: photocatalytic reaction

$$\text{Dye(adsorbed)} \longrightarrow \text{products(slow)} \tag{3}$$

It can be assumed that the first step occurs until equilibrium, whereas the second is rate limiting.

For the first step, the equilibrium adsorption capacity q_e (mg·g^{-1}) can be calculated according to

$$q_e = V \cdot \frac{C_0 - C_e}{m}, \tag{4}$$

where C_0 and C_e are the initial and equilibrium dye concentrations (mg·L^{-1}); V and m are the solution volume (L) and mass of catalyst (g), respectively.

Further, C_e and q_e are related following the Langmuir isotherm.

$$q_e = q_m \cdot \frac{K_L \cdot C_e}{1 + K_L \cdot C_e}, \tag{5}$$

where q_m (mg·g^{-1}) and K_L (L·mg^{-1}) are the maximum monolayer adsorption capacity and the Langmuir equilibrium constant, respectively.

The photocatalytic degradation rate can be expressed by

$$r = k_r \cdot \theta, \tag{6}$$

where k_r is the apparent rate constant (mg·L^{-1}·min^{-1}) and θ is the coverage fraction (dimensionless), which can be represented by the Langmuir isotherm. Therefore, equation (6) can be rewritten as

$$r = k_r \cdot \frac{K_L \cdot C}{1 + K_L \cdot C} = -\frac{dC}{dt}. \tag{7}$$

Now, integrating equation (7) with the boundary conditions of $C = C_e$ at $t = 0$ min (subtracted the time required for saturated adsorption) and $C = C$ at $t = t$.

$$\frac{1}{K_L} \cdot \ln C + C = -k_r \cdot t + \frac{1}{K_L} \cdot \ln C_e + C_e. \tag{8}$$

The values of k_r can be obtained from the slope of the linear plot $((1/K_L) \cdot \ln C + C)$ vs. t.

3. Results and Discussion

3.1. Synthesis of the Porous Octahedral ZnO/CuO Composite from Zn/Cu-BTC. The compositional phase of the as-prepared materials is investigated using XRD (Figure 1). The reflection peaks of Cu-BTC appear as (200), (220), (311), (222), (400), (331), (420), (422), (511), (440), (600), (444), (511), (553), and (751) [32, 33], which indicates that the obtained Cu-BTC is MOF-199 with a space group of $Fm\bar{3}m$ [13]. Zn-BTC can exist in different forms depending on the synthesis conditions. The XRD pattern of the prepared Zn-BTC is consistent with that of Zn-BTC synthesized with the microwave-assisted method [21] but is different from that synthesized from $Zn(CH_3COO)$ with the solvothermal method [17] and with the ultrasound-assisted method [18]. The XRD patterns of Zn/Cu-BTC are consistent with those of Cu-BTC with a characteristic peak of Zn-BTC at 10.5°, indicating that Zn/Cu-BTC is constituted from Cu-BTC and Zn-BTC.

The thermal behaviors of BTC compounds are studied via TG-DTA (Figure 2). For Zn-BTC and Cu-BTC, an exothermic peak appears at around 472 and 327°C, respectively, accompanied by large weight losses (approximately 42 and 39%), which is attributed to the combustion of BTC in the compounds (see Table S1). The complete decomposition temperature is around 470°C for Cu-BTC (400°C reported by reference [34], 670°C reported by reference [35]) and 500°C for Zn-BTC. In the case of Zn/Cu-BTC, an endothermic peak at 100°C with a weight loss of approximately 27% is assigned to the evaporation of the physically adsorbed water. Two exothermic peaks at 334 and 387°C with a weight loss of around 47% are due to the decomposition of Cu-BTC and Zn-BTC in Zn/Cu-BTC. The complete decomposition of Zn/Cu-BTC also takes place at around 500°C, and therefore, this temperature is selected to calcinate the precursors to obtain the oxides.

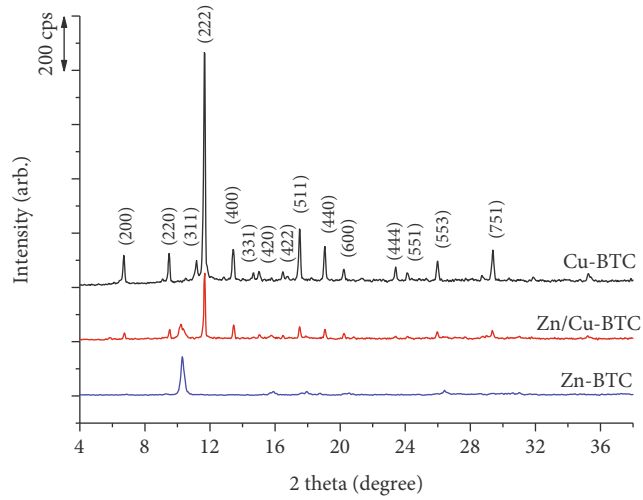

Figure 1: XRD patterns of Cu-BTC, Zn-BTC, and Zn/Cu-BTC.

During the calcination for 5 hours, hexagonal wurtzite ZnO, monoclinic CuO (JCPDS card No. 48–1548 and 36–1451, respectively), and bimetallic ZnO/CuO are formed (Figure 3). No unknown peaks are observed in the XRD diagrams, indicating that pure single oxides and a bimetallic oxide (ZnO/CuO) are obtained. In addition, the presence of peak broadening reveals that a grain refinement occurs in ZnO/CuO possibly due to the formation of heterojunction structures. The average particle size of ZnO and CuO in the octahedral ZnO/CuO nanocomposite is ~44 nm and ~23 nm (calculated using Scherrer's equation from the line broadening of (101) and (111) diffraction peak for ZnO and CuO, respectively).

Figure 4 displays the morphologies of the as-prepared materials before and after calcination. Cu-BTC yields smooth octahedral crystals of ~10 μm size (Figure 4(a1)); however, during calcination, the structural framework of Cu-BTC collapses to form irregular particles (Figure 4(a2)). To prevent this collapse, the calcination temperature was set to ~400°C (Figure S1). Zn-BTC comprises nanorods of diameter ~200 nm (Figure 4(b1)), and after calcination, they yield in ZnO nanofibers (consisted of nanoparticles of 30~50 nm size) (Figure 4(b2)). As for Zn/Cu-BTC, octahedral particles with flocculent substances (Zn-BTC) on the crystal surface are formed (Figure 4(c1)). Bimetallic ZnO/CuO octahedrons of diameter 5–10 μm remain unaltered after calcination (Figure 4(c2)). The TEM images show that ZnO/CuO octahedrons comprise nanoparticles of ~50 nm size (Figure 4(d1)). On the HR-TEM images of ZnO/CuO, it can be seen that the interplanar spacing of lattice fringes is 0.232 nm (corresponding to the (111) plane of monoclinic CuO (JCPDS card No. 48–1548)) and 0.281 nm (corresponding to the (100) plane of hexagonal ZnO (JCPDS card No. 36–1451)). Hence, the intragranular location of both oxide phases could enhance the efficiency of semiconductor coupling effects.

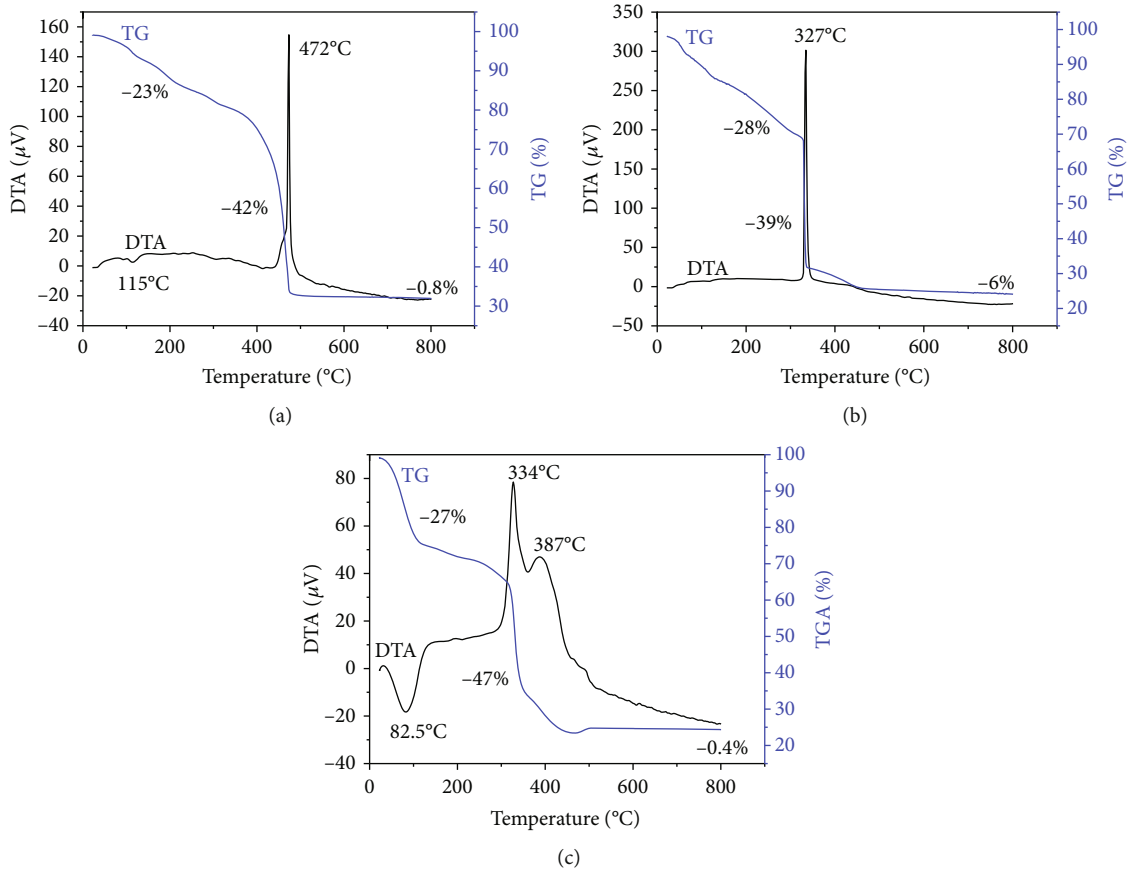

Figure 2: TG-DTA diagrams of (a) Zn-BTC, (b) Cu-BTC, and (c) Zn/Cu-BTC.

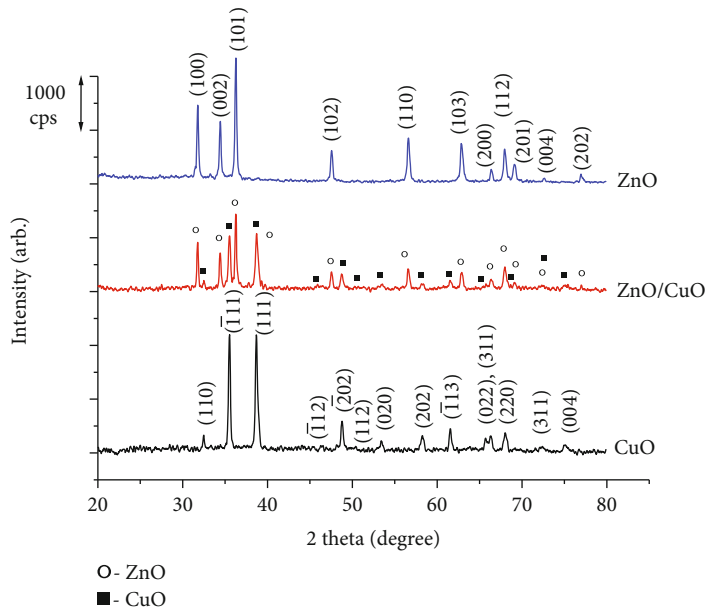

Figure 3: XRD patterns of ZnO, CuO, and ZnO/CuO.

The elemental analysis of C, H, Zn, and Cu in the as-prepared materials is presented in Table 1. No carbon is present in ZnO/CuO, indicating the complete removal of the organic templates. The molar ratio of Zn/Cu in Zn/Cu-BTC and ZnO/CuO analyzed with AAS and EDX (Figure S2) is practically identical (0.42/1 and 0.39/1 for

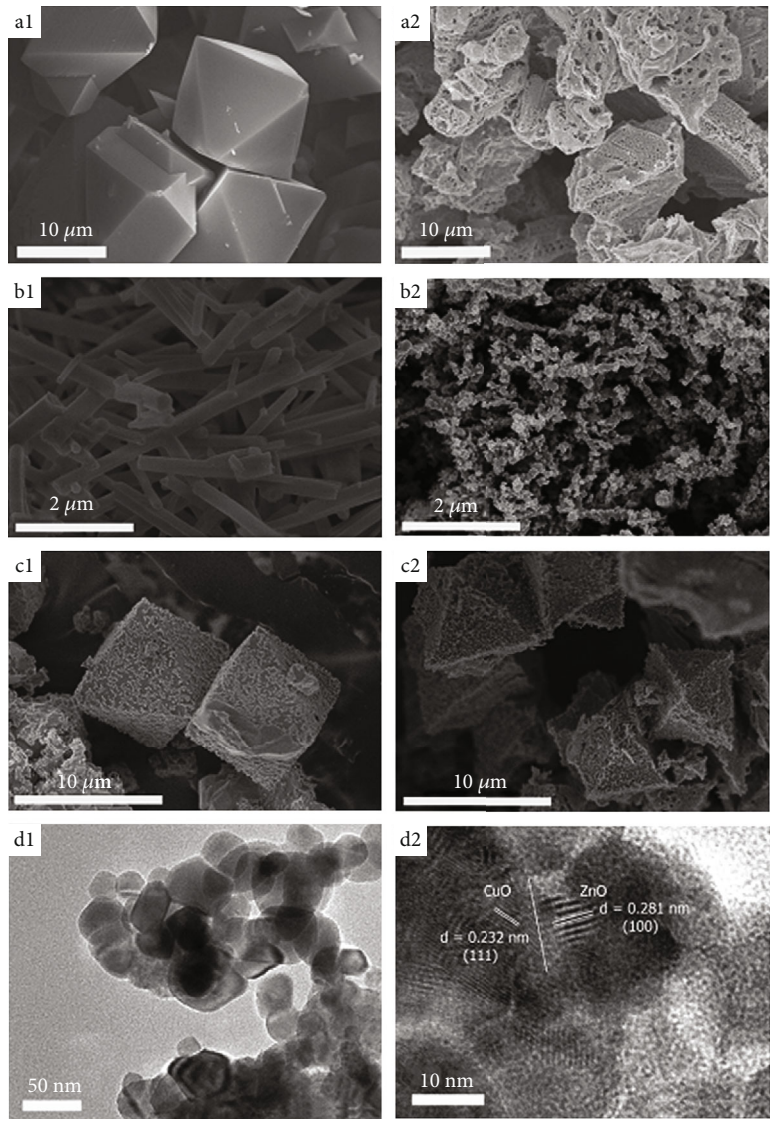

Figure 4: SEM observations of (a1) Cu-BTC, (b1) Zn-BTC, (c1) Zn/Cu-BTC, (a2) CuO, (b2) ZnO, and (c2) ZnO/CuO; (d1) TEM observation of ZnO/CuO; (d2) HR-TEM of ZnO and CuO region.

Table 1: Elemental analysis of C, H, Zn, and Cu in Zn/Cu-BTC and ZnO/CuO.

Notation	Elemental composition (% mass)				Zn/Cu (mol/mol)	
	C*	H*	Zn**	Cu **	(**)	(***)
Zn/Cu-BTC	36.18	1.93	7.49	17.19	0.42/1	0.39/1
ZnO/CuO	0.00	0.00	20.18	62.56	0.31/1	0.30/1

*Elemental analysis; **AAS analysis; ***EDX analysis.

Zn/Cu-BTC and 0.31/1 and 0.30/1 for ZnO/CuO), implying a high dispersion of bimetallic oxides. However, this molar ratio is significantly lower than the initial one (Zn/Cu = 7/3 = 2.33/1), signifying that a large number of Zn^{2+} ions remain in the solution instead of transforming into ZnO. It might happen due to the lower affinity of Zn (electronegativity, 1.65) to carboxyl groups in BTC compared with that of Cu to BTC (electronegativity, 1.9).

The textural properties of the as-synthesized materials were investigated using nitrogen adsorption/desorption isotherms (Figure 5). According to IUPAC, the obtained BTC compounds can be assigned to I-type (microporous materials) [36, 37]. BTC compounds except Zn-BTC exhibit a large surface area as those published in the literature [13]. The BET surface areas of Cu-BTC, Zn-BTC, and Zn/Cu-BTC are 1635 $m^2 \cdot g^{-1}$, 3 $m^2 \cdot g^{-1}$, and 844.4 $m^2 \cdot g^{-1}$, respectively (see Table S2). Feldblyum et al. [20] asserted that the low surface area of Zn-BTC is because of its densified surface crystal, presumably due to pore collapse. The blocking of large pores at the surface effectively inhibits adsorbates such as N_2 gas from entering the bulk structure [20]. After calcination, the isotherm of ZnO remains in type I, while the other oxides exhibit the type-IV isotherm with an H3

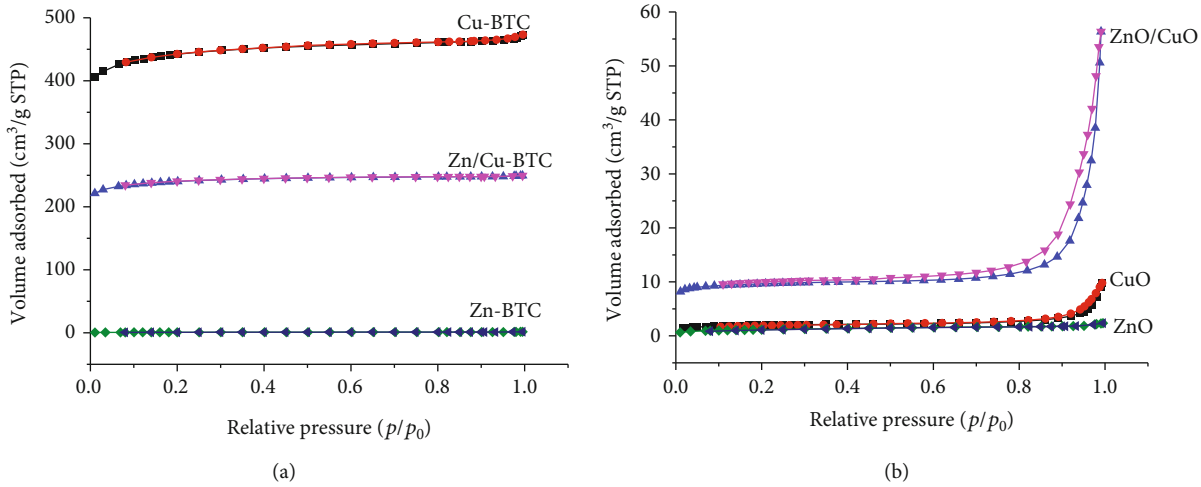

Figure 5: Nitrogen adsorption/desorption isotherms of Cu-BTC, Zn-BTC, Zn/Cu-BTC, CuO, ZnO, and ZnO/CuO.

hysteresis loop at a relative pressure ranging from 0.5 to 0.9, manifesting the presence of mesopores and micropores [36, 38]. The specific surface area of calcined materials except ZnO reduces significantly to 6.7 $m^2 \cdot g^{-1}$ for CuO and 32.5 $m^2 \cdot g^{-1}$ for ZnO/CuO. It is worth noting that the specific surface area of the octahedral ZnO/CuO nanocomposite in this study is significantly higher than that of ZnO and CuO and approximately two to four times as high as that of several ZnO/CuO composites synthesized with other methods [7, 39, 40]. This result confirms the advantages of synthesizing multimetal oxide from MOF precursors.

The XPS spectra of the ZnO/CuO nanocomposite are presented in Figure 6. The survey spectrum shows that the presence of Zn, Cu, and O without any foreign species except for carbon whose 1s peak (284 eV) is employed to calibrate the acquired spectra (Figure 6(a)). The XPS spectrum of Cu has a doublet of $Cu2p_{3/2}$ (at 933 eV) and $Cu2p_{1/2}$ (at 952 eV) along with other satellite peaks at higher binding energies [39] (Figure 6(b)). Both peaks are very typical for the XPS spectrum of Cu^{2+} [28]. Zn(II) manifests a doublet of $Zn2p_{3/2}$ at 1022 eV and $Zn2p_{1/2}$ at 1045 eV (Figure 6(c)) [41]. Therefore, it can be inferred that ZnO/CuO is a compound containing Zn (II), Cu (II), and O.

The band gap energies (E_g) of ZnO, CuO, and ZnO/CuO are calculated using UV-Vis-DRS measured at room temperature (Figure 7(a)). ZnO exhibits an absorption band with wavelengths of 350–390 nm (band gaps of 3.5–3.2 eV) in the ultraviolet region. CuO manifests a broad peak in the visible light region. The characteristic absorption bands of ZnO and CuO are observed in the spectrum of ZnO/CuO. The absorption band of CuO shifts toward shorter wavelengths and integrates with the absorption band of ZnO, signifying that the band edges of *p*-type CuO and *n*-type ZnO are well-matched [8]. Tauc's plot [42] is illustrated in Figure 7(b). The E_g values of ZnO and CuO are 3.19 eV and 1.94 eV, respectively (previously reported as 3.2–3.3 eV for ZnO [43, 44] and 1.4–1.85 eV for CuO [44–46]) (see Table S3). ZnO/CuO has an E_g value of 2.63 eV, manifesting a remarkable shift toward the longer wavelength region.

Figure 8 shows the photoluminescence spectra (PL) of the obtained materials with an excitation wavelength of 300 nm. The maximum PL intensity is at 387.4 nm for CuO and 510.2 nm for ZnO. However, the PL intensity of ZnO/CuO composite is significantly weaker than those of the CuO and ZnO. It is well known that low PL intensity means low recombination of electron and holes, then the opposite would be high PL intensity would increase recombination rate and reduce photocatalytic activity. These results demonstrate that the combinations ZnO and CuO have reduced the recombination of photonic electrons and photogenic holes, which may increase the photocatalytic activity of the material.

3.2. Visible-Light-Driven Photocatalytic Degradation of Dyes

3.2.1. Decolorization of MB with Different Catalysts. Figure 9(a) displays the process of MB decolorization over Zn-BTC, Cu-BTC, and Zn/Cu-BTC. It is apparent that the adsorption equilibrium is reached after 60 min, and the BTC compounds exhibit high adsorption capacities. Zn/Cu-BTC displays the highest decolorization efficiency (F) at ~69%, followed by Cu-BTC (~66%) and Zn-BTC (~22%) ($F = 100 \times (C_0 - C_t)/C_0$, where C_0 and C_t are the initial concentration and at time t). However, the decolorization efficiency of Cu-BTC decreases to 41–50% after 60 min of UV/Vis irradiation. This indicates that desorption occurs during irradiation. Zn-BTC exhibits weak photocatalytic activity upon UV or Vis irradiation and yields a decolorization efficiency of ~50% after 420 min of UV illumination and 38% after 420 min of Vis irradiation. This may be due to its very low surface area which decreases the number of active sites for MB to adsorb and decompose.

In contrast, all calcinated materials manifest poor adsorption with a very low decolorization efficiency of ~5%. This is

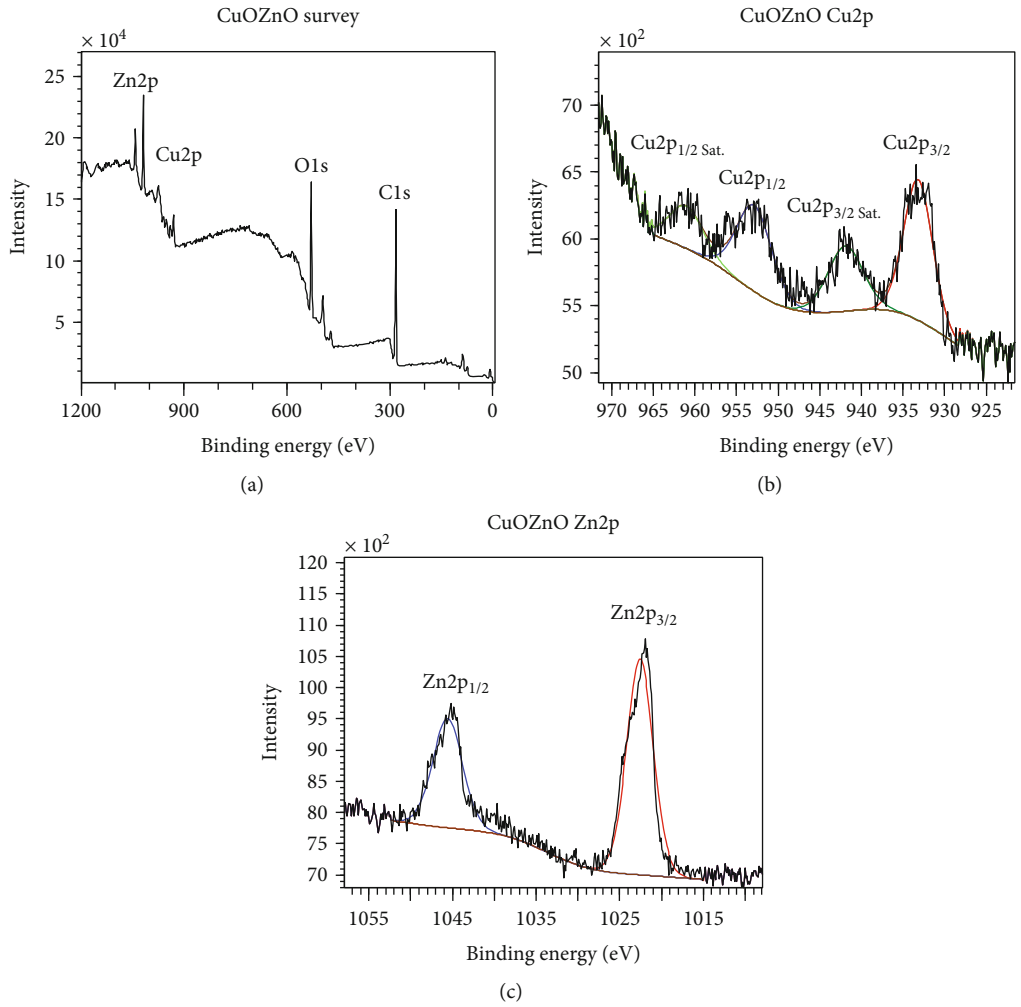

Figure 6: XPS spectra of ZnO/CuO (a) survey spectrum, (b) Cu2p where Sat denoted as satellite peaks, and (c) Zn2p1/2 spectrum.

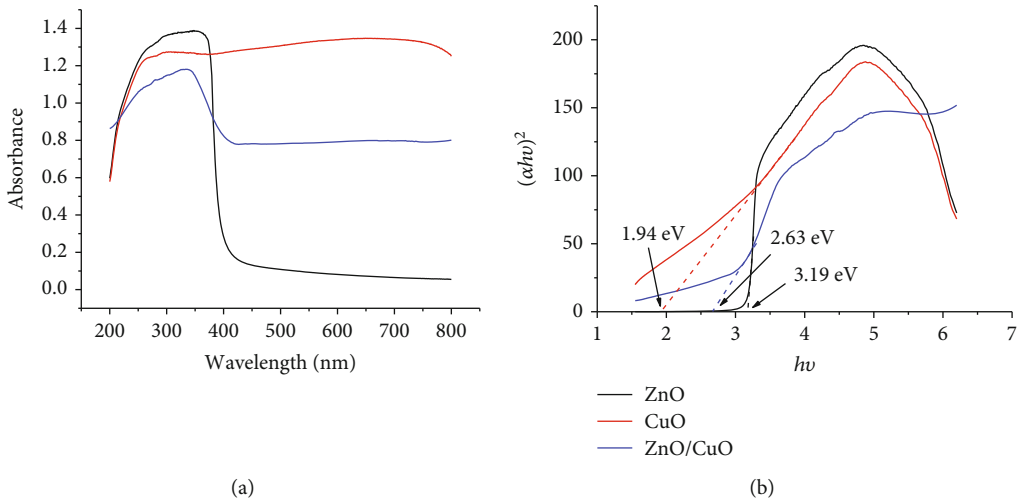

Figure 7: (a) UV-Vis diffuse reflectance spectra and (b) Tauc's plots of ZnO, CuO, and ZnO/CuO.

the result of the collapse of the porous structure after calcination, leading to the disappearance of the adsorption sites. As can be seen from Figure 9(b), CuO could not catalyze any MB degradation, while ZnO and ZnO/CuO exhibit photocatalytic activities in both visible and ultraviolet regions. It is worth noting that ZnO/CuO demonstrates an excellent

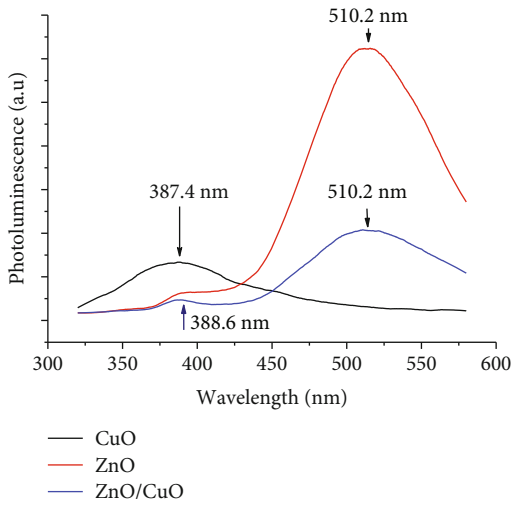

Figure 8: Photoluminescence spectra of CuO, ZnO, and ZnO/CuO.

photocatalytic activity, and the complete decolorization of MB occurs after 120 min under visible illumination. Meanwhile, ZnO (UV) and ZnO (Vis) decolorize MB up to 95 and 90%, respectively, after 240 min of illumination. The ZnO/CuO composite also catalyzes MB degradation faster than pure CuO or ZnO under visible light illumination. In fact, after 120 minutes, its decolorization efficiency is 1.57 and 7.7 times as high as that of ZnO and CuO, respectively. The porous ZnO/CuO composite with a large surface area would provide the heterojunction structure and an effective environment for a larger number of surface active sites. This increases MB–ZnO/CuO interaction and thus promoting photodegradation. In other words, the combination of ZnO and CuO causes the synergistic effect in the catalytic degradation of methylene blue.

3.2.2. Effect of pH and Leaching Experiment. Effect of pH on decolorization of MB over ZnO/CuO catalyst is shown in Figure 10(a). The decolorization performance seems to be unchangeable in pH range from 2 to 7 and increases significantly when pH increases. The point of zero charge (pH_{pzc}) for ZnO/CuO, determined using the pH drift method, is around 7.9 (Figure 10(b)) [47]. At lower pH (lower than pH_{pzc}), the surface of ZnO/CuO is positively charged. When pH increases from 2 to 7, the surface becomes less positive and the decolorization efficiency increases slightly. At higher pH (higher than pH_{pzc}), the surface of ZnO/CuO is negatively charged; hence, MB and the catalyst attract each other through electrostatic interaction; thus, the decolorization efficiency increases significantly.

During the leaching experiment, the catalyst was filtered after 30 min and the decolorization of MB under illumination almost stops (Figure 10(c)). In addition, the decolorization of MB without the catalyst is not observed after 70 min of illumination, indicating that MB is stable in the visible light region. Therefore, it can be inferred that ZnO/CuO acts as a heterogeneous catalyst in the photocatalytic degradation of methylene blue.

3.2.3. Visible-Light-Driven Photocatalytic Degradation of MB with ZnO/CuO Composite. The absorption bands at 292 nm and at 664 nm on the UV-Vis absorption spectra of MB can be attributed to the benzene ring and the conjunction color group –N=N–, respectively (Figure 11(a)). The intensity of these bands decreases with the increasing illumination time, and they almost disappear after 90 min of the reaction. The decolorization of MB occurs due to the disappearance of the color conjunction group during illumination. The TOC test also proves the mineralization of MB during photocatalytic degradation (Figure 11(b)). The TOC of MB reduces significantly from 6.35 $mg{\cdot}L^{-1}$ for initial solution to 0.72 $mg{\cdot}L^{-1}$ after 140 min of illumination, indicating complete mineralization of MB over ZnO/CuO composite.

In order to clarify the radical mechanism of the degradation reaction, three radical scavengers (KI for electron holes, isopropanol for $^{\cdot}OH$, and benzoquinone for $O^{2\cdot-}$) were used in the present experiment. It is evident that the addition of isopropanol causes a moderate reduction in photocatalytic activity, while KI practically impedes the photocatalytic degradation of MB (Figure 12). Benzoquinone hinders degradation by around 50%. This infers that electron holes and superoxides play an important role in MB degradation.

A mechanism of photocatalysis on a semiconductor is employed to explain the photocatalytic activities in the visible light region. Since the band gap positions for the conduction band of CuO and ZnO are −0.43 eV and −0.15 eV *vs.* NHE, respectively [9, 48], and the band gaps of CuO and ZnO are 1.94 and 3.19 eV, then the band gap positions for valence bands are 1.51 eV for CuO and 3.04 eV for ZnO (see Table S3). Due to the strong light adsorption capacity of CuO in the visible light region, electrons are excited from VB to CB to form photogenerated h^+/e^- pairs. The position of CB in CuO is more negative than that in ZnO; hence, the transfer of the excited electrons to E_{CB} (ZnO) prevents the fast recombination of photoexcited e^-/h^+ pairs (equations (9) and (10)). On the other hand, the state of MB (1.17 eV) could be excited to MB* (−0.69 eV) by visible light [49, 50] (equation (11)). The work function of the photoexcited MB* (−0.69 eV) is more negative than that of CuO and ZnO [49, 50]. MB acts as the photosensitizer to provide additional photogenerated electrons into CBs of CuO and ZnO through the formed downstream channel (equations (12) and (13)). The VB potential for CuO (1.51 eV) is more positive than that of MB (1.17 eV); therefore, h^+ could easily oxidize MB to form degradation products (equation (14)). On the other hand, the CB edge position of CuO (−0.43 eV) is more negative than that of E^0 $(O_2/O_2^{\cdot-})$ (−0.33 eV) [51]; thus, electrons on the conduction band of CuO reacts with O_2 to produce superoxide radical $O_2^{\cdot}$, which could substantially oxidize MB to form degradation products (equations (15) and (16)). In principle, h^+ (1.51 eV) could not oxidize H_2O ($E(H_2O/^{\cdot}OH) = 2.6$ eV), but the experimental result still indicates the role of $^{\cdot}OH$ in the oxygenation of dye as shown in Figure 12. This is still a challenging problem possibly due to the deviation between theoretical and practical estimation. The transfer path of

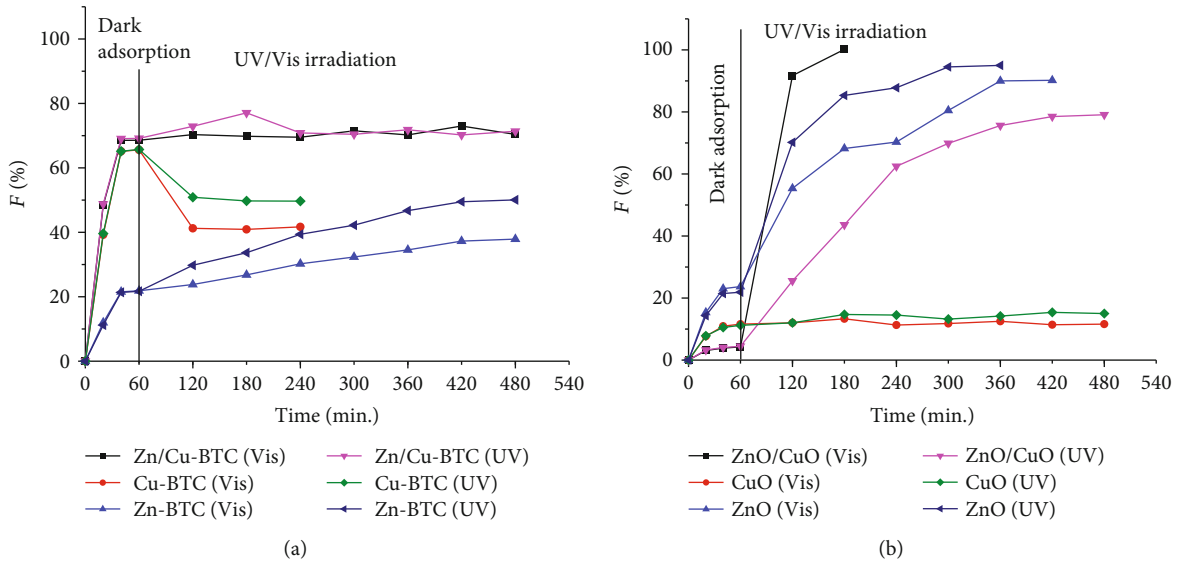

FIGURE 9: Decolorization of MB over (a) as-prepared Zn-BTC, Cu-BTC, Zn/Cu-BTC, and (b) CuO, ZnO, and ZnO/CuO under UV and visible irradiation (conditions: $V = 500$ mL; $m_{catalyst} = 400$ mg; concentration of MB = 10 ppm).

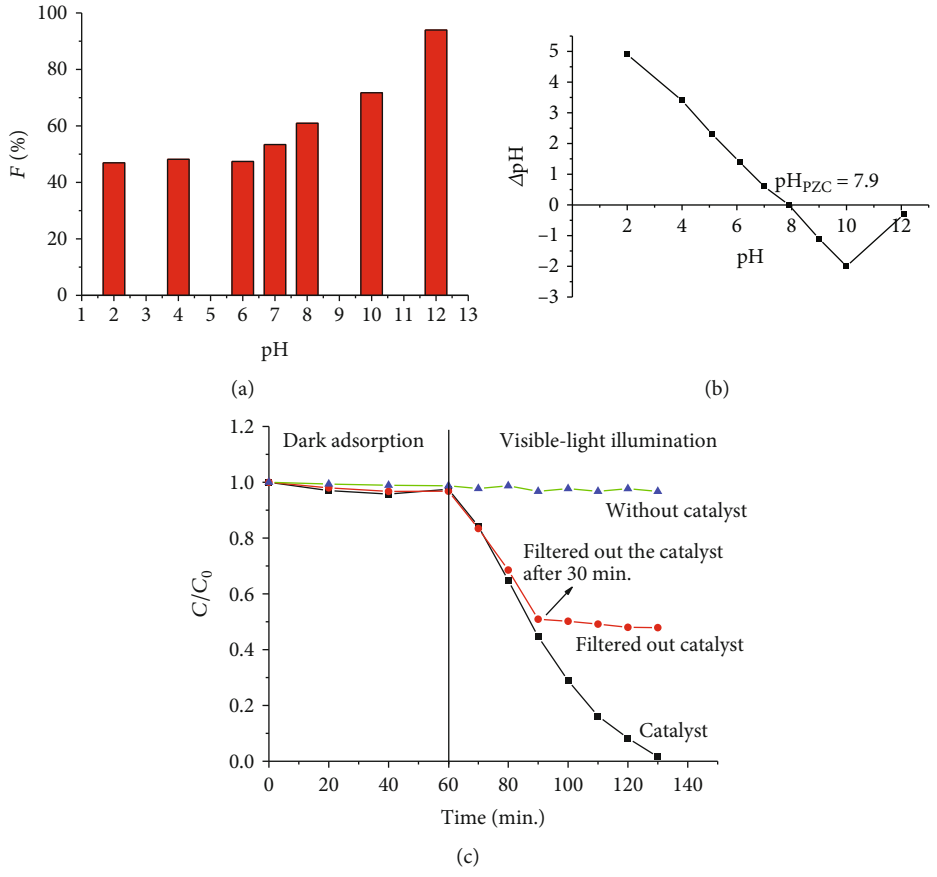

FIGURE 10: (a) Effect of pH on decolorization of MB over porous ZnO/CuO octahedron catalyst; (b) the point of zero charge obtained from the pH drift method ($V = 100$ mL, $C_0 = 10$ mg · L^{-1}; $m_{catalyst} = 80$ mg; adsorption time = 60 min; illumination time = 70 min); (c) leaching experiment ($V = 500$ mL; $C_0 = 10$ mg · L^{-1}; $m_{catalyst} = 400$ mg, adsorption time = 60 min).

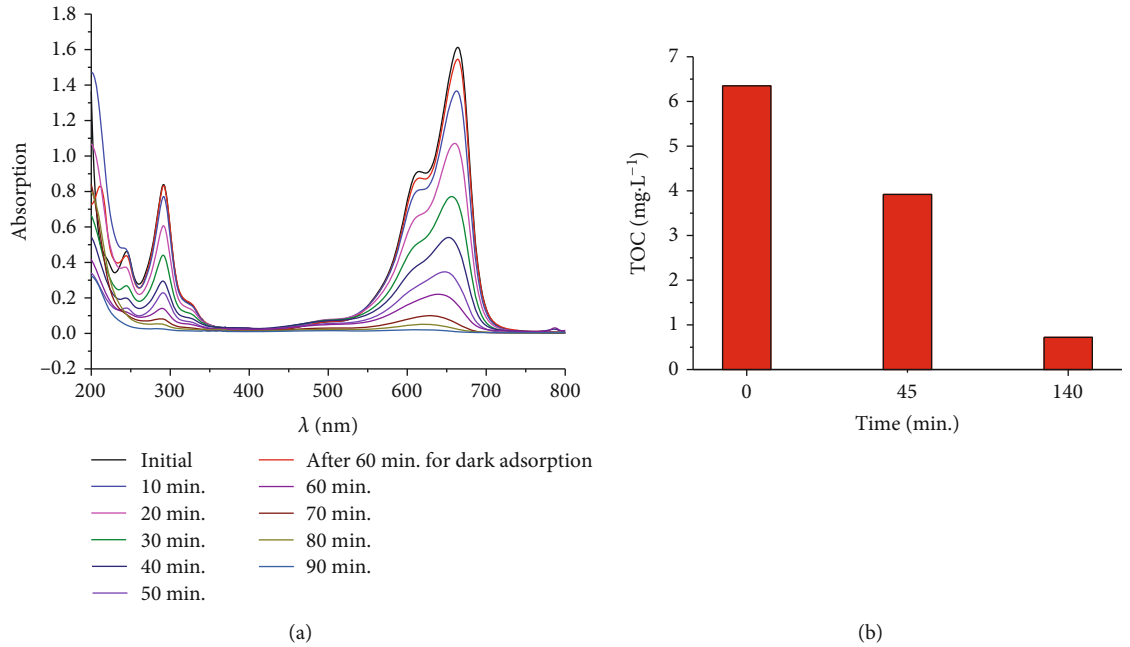

Figure 11: (a) UV-Vis absorption spectra at different times and (b) TOC of MB solution in the photocatalytic degradation ($V = 500$ mL; $C_0 = 10$ ppm; $m_{catalyst} = 400$ mg; adsorption time = 60 min).

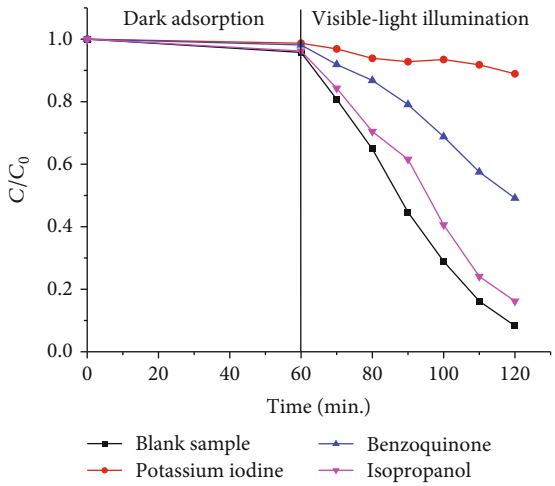

Figure 12: Effect of radical scavengers (potassium iodide, isopropanol, and benzoquinone) on MB decolorization over porous ZnO/CuO octahedrons catalyst ($V = 100$ mL; $C_0 = 10$ ppm; $m_{catalyst} = 80$ mg; adsorption time = 60 min; concentration of scavenger solution: 2.4×10^{-4} M).

photogenerated charge carriers under visible light illumination is illustrated in Figure 13.

$$\mathrm{ZnO/CuO} + h\nu \longrightarrow \mathrm{ZnO/CuO}\left(\mathrm{h^+ + e^-}\right) \quad (9)$$

$$\mathrm{ZnO/CuO}\left(\mathrm{e^-/CB}\right) \longrightarrow \left(\mathrm{e^-/CB}\right)\mathrm{ZnO/CuO} \quad (10)$$

$$\mathrm{MB} + h\nu \longrightarrow \mathrm{MB^*} \quad (11)$$

$$\mathrm{MB^*} \longrightarrow \mathrm{e^- + MB^{*+}} \quad (12)$$

$$\mathrm{MB^{*+}} \longrightarrow \mathrm{MB + h^+} \quad (13)$$

$$\mathrm{CuO}\left(\mathrm{h^+}\right) + \mathrm{MB} \longrightarrow \text{degradation products} \quad (14)$$

$$\mathrm{CuO}\left(\mathrm{e^-/CB}\right) + \mathrm{O_2} \longrightarrow \mathrm{O_2^{\bullet -}} + \mathrm{ZnO} \quad (15)$$

$$\mathrm{O_2^{\bullet -}} + \mathrm{MB} \longrightarrow \text{degradation products} \quad (16)$$

3.2.4. Kinetics of MB Photocatalytic Degradation. The kinetics of adsorption and photocatalytic degradation is presented in Figure 14(a). It is evident that the adsorption reaches equilibrium after 60 min in the dark (MB concentrations of 5~30 ppm). The values of the maximum monolayer adsorption capacity (q_m) and the Langmuir equilibrium constant (obtained from the nonlinear plot of q_e vs. C_e (equation (5))) are 1.63 mg·g^{-1} and 0.047 L·mg^{-1}, respectively (Figure S3 and Table S4). Equation (8) becomes

$$\frac{1}{0.047} \cdot \ln C + C = -k_r \cdot t + \frac{1}{0.047} \cdot \ln C_e + C_e. \quad (17)$$

The values of k_r can be calculated from the slope of equation (17) ($((1/0.047) \times \ln C + C)$ vs. t, Figure 14(b) and Table 2). The classical kinetic model (*pseudo*-first-order-kinetic model) in the linear form as equation (1) is employed to analyze the kinetic data for comparing the goodness of fit (Table 2). The paired sample t test with $\alpha = 0.05$ shows that the proposed model provides statistically higher determination coefficients than the *pseudo*-first-order kinetic model ($t(4) = 5.899$, p value = 0.002 (<0.05)), indicating that the proposed model fits the data more accurately than the classical kinetic model.

It is difficult to compare the catalytic activity of ZnO/CuO composite in the present with that of other catalysts

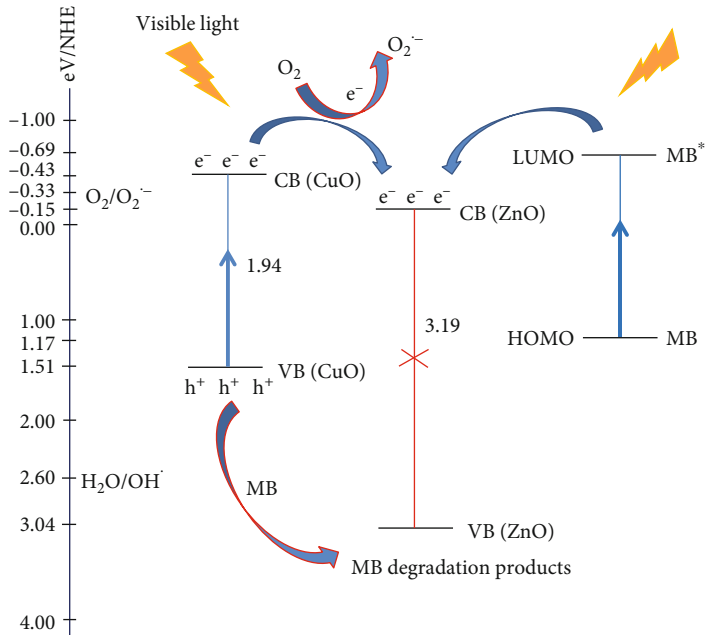

FIGURE 13: Energy of valence band edge and conduction band edge for ZnO/CuO coupling semiconductor (HOMO: highest occupied molecular orbital and LUMO: lowest unoccupied molecular orbital).

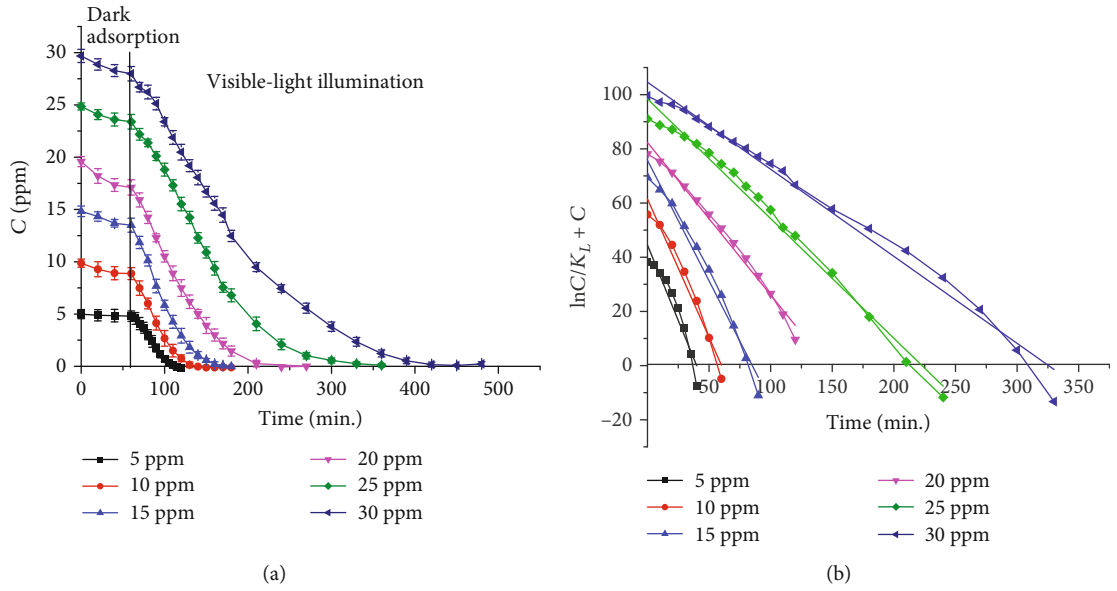

FIGURE 14: (a) Kinetics of adsorption and photocatalytic degradation of methylene blue over octahedral ZnO/CuO catalyst; (b) linear plots of the proposed kinetic model (conditions: $V = 500$ mL, $C_0 = 5 - 30$ mg · L^{-1}, $m_{catalyst} = 400$ mg, temperature = 35°C).

previously reported due to different light sources (UV or Vis), the initial concentration of reactants, the amount of catalyst, the reaction volume, etc. The *pseudo*-first-rate constant appears to be relevant because several authors report the catalytic activity in terms of this value (Table 3). The value of the *pseudo*-first-rate constant for the degradation on the present catalyst in the visible region is lower than that for graphene-like carbon/TiO_2 and ZnO/graphene oxide in the UV region and compatible with commercial P25, but higher than that for other catalysts reported such as Ta-ZnO, g-C_3N_4/CdS, and Ce-TiO_2.

3.2.5. Recyclability. Recyclability is an important factor in heterogeneous catalysis. After the cycling experiment, the ZnO/CuO catalyst was first separated by centrifugation, then washed with water and ethanol for three times to remove the dye, and finally dried at 120°C for 15 h. The photocatalytic degradation efficiency of ZnO/CuO decreases from 100% to 97.2% after three cycles (Figure 15(a)). The XRD patterns of the recycled ZnO/CuO samples stay unaltered; therefore, it can be inferred that ZnO/CuO remains stable during photocatalytic degradation reactions (Figure 15(b)).

Table 2: Determination coefficients of the proposed model in the linear form and apparent rate coefficients.

Initial MB concentration C_0 (mg·L^{-1})	R^2 (proposed model)	Apparent rate coefficient, k_r (mg·L^{-1}·min^{-1})	R^2 (*pseudo*-first-order kinetic model)	*Pseudo*-rate constant k (min^{-1})
5	0.919	1.1138	0.8303	0.0721
10	0.968	1.0219	0.8832	0.0532
15	0.978	0.8909	0.9146	0.0447
20	0.988	0.5629	0.8816	0.0367
25	0.988	0.4417	0.9630	0.0179
30	0.986	0.3213	0.9330	0.0132

Table 3: Comparison of the *pseudo*-first-order rate constant of the present catalyst with that of other catalysts.

Catalyst	S_{BET} (m^2·g^{-1})	Light source (nm, power)	C_0 (mg·L^{-1})/volume (mL)/ $m_{catalyst}$ (mg)	Pseudo-first-order rate constant, k (min^{-1})	References
ZnO	8.21	UV, 20 W	10/100/50	0.022	[52]
ZnO/graphene oxide	31.58	UV,20 W	10/100/50	0.098	[52]
Pristine TiO_2 (P25)	—	254, 11 W	10/100/50	0.009	[53]
Graphene-like carbon/TiO_2	—	254, 11 W	10/100/50	0.248	[53]
Pristine TiO_2 (P25)	51	≤370, 18 W	9.6/100/50	0.043	[54]
Sm-TiO_2	46	370, 18 W	9.60/100/50	0.020	[54]
Ce-TiO_2	46	370, 18 W	9.60/100/50	0.024	[54]
TiO_2	50	340, 125 W	23/2750/375	0.025	[55]
CdS	111.2	>420, 500 W	25/200/80	0.0079	[56]
g-C_3N_4	9.8	>420, 500 W	25/200/80	0.0039	[56]
g-C_3N_4-CdS	166.5	>420, 500 W	25/200/80	0.0121	[56]
Ag/ZnO	—	>570 (high pressure sodium lamp)	5/–/150	0.006	[57]
Ta-ZnO	36	>420, 300	10/50/50	0.0401	[58]
CeO_2-TiO_2	66	>420, 160	10/100/80	0.0341	[59]
ZnO/CuO	33	>420, 160	10/500/400	0.0532	This work

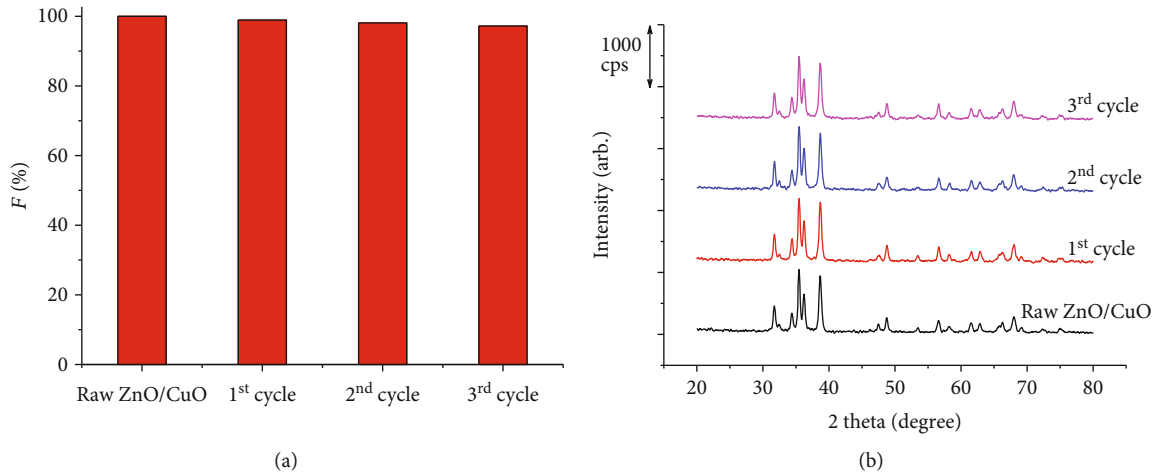

Figure 15: (a) Photocatalytic degradation efficiency of used catalysts; (b) XRD patterns of ZnO/CuO after the third cycle (V = 1000 mL, C_0 = 10 ppm, $m_{catalyst}$ = 800 mg; adsorption time = 60 min; light illumination time = 80 min).

In addition, the obtained catalyst manifests excellent photocatalytic degradation of several other dyes, including phenol, phenol red, methyl orange, and Congo red (Figure 16). Porous octahedral ZnO/CuO composite exhibits superior visible-light-driven photocatalytic degradation of MB compared with single CuO or ZnO.

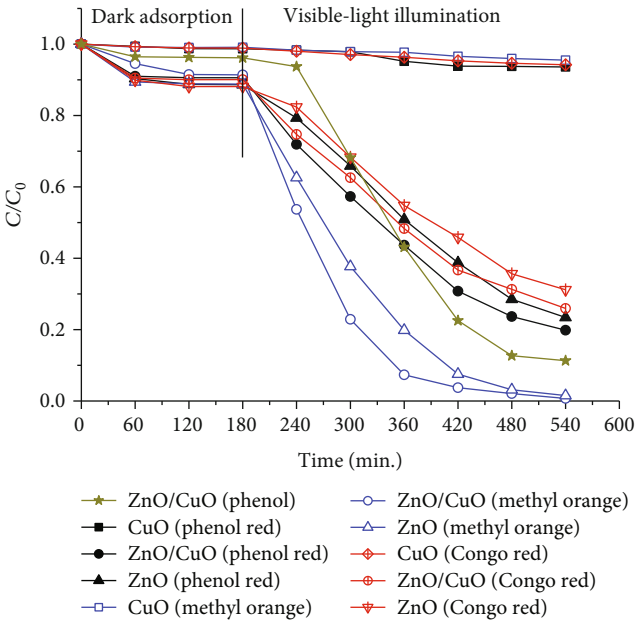

FIGURE 16: Visible-light driven photocatalytic degradation of several dyes over ZnO, CuO, and porous octahedral ZnO/CuO composite (condition: concentration of dyes = 10 ppm; V = 500 mL; $m_{catalyst}$ = 400 mg; illumination time = 540 min).

4. Conclusions

In this study, a porous octahedral ZnO/CuO composite was synthesized from Zn/Cu-based MOF-199. The fabricated ZnO/CuO composite possesses a hierarchical 3D structure consisted of porous octahedral particles of 5–10 μm in size. Compared with pure ZnO and CuO, the as-prepared ZnO/CuO composite exhibits superior photocatalytic degradation of phenol and different dyes (methyl blue, methyl orange, phenol red, and Congo red) in the visible light region. The formation of a stable p–n junction that efficiently separates the photogenerated electron-hole pairs within each semiconductor material is responsible for the degradation. The synthesized photocatalyst remains stable after four cycles of application. The kinetic model of photocatalytic degradation with a unimolecular reaction over heterogeneous catalyst combined with the Langmuir adsorption isotherm is proposed. This model is statistically consistent with the experimental data. The porous ZnO/CuO octahedron composite is an active and stable visible-light-driven catalyst and may serve as a potential catalyst for practical use in the treatment of dye pollutants in aquatic effluents.

Data Availability

The data used to support the findings of this study are available from the corresponding author upon request.

Conflicts of Interest

The authors declare that they have no conflicts of interest.

Acknowledgments

This research was sponsored by Hue University under Decision No. 1208/QĐ-DHH.

Supplementary Materials

Table S1 presents the weight loss and temperature range derived from TG–DTA measurement of Cu-BTC, Zn-BTC, and Zn/Cu-BTC. The specific surface areas calculated by using the BET model, porous diameters, and volumes for the resulting materials were obtained from the analysis of nitrogen adsorption isotherm data (Table S2). Band gap energy and band edge position of CuO, ZnO, and ZnO/CuO calculated by using Tauc's equation are listed in Table S3. The parameters of the Langmuir and Freudlich isotherm models in linear forms are listed in Table S4 and illustrated in Figure S3. CuO prepared by the pyrolysis of Cu-BTC at 400°C for 5 h retained the octahedral particles as intimal Cu-BTC (Figure S1). The EDX measurement revealed that zinc and copper coexisted in ZnO/CuO sample. *(Supplementary Materials)*

References

[1] A. Janotti and C. G. Van de Walle, "Fundamentals of zinc oxide as a semiconductor," *Reports on Progress in Physics*, vol. 72, no. 12, article 126501, 2009.

[2] D. C. Reynolds, D. C. Look, and B. Jogai, "Optically pumped ultraviolet lasing from ZnO," *Solid State Communications*, vol. 99, no. 12, pp. 873–875, 1996.

[3] Z.-L. Liu, J.-C. Deng, J.-J. Deng, and F.-F. Li, "Fabrication and photocatalysis of CuO/ZnO nano-composites via a new method," *Materials Science and Engineering: B*, vol. 150, no. 2, pp. 99–104, 2008.

[4] C. Xu, L. Cao, G. Su et al., "Preparation of ZnO/Cu_2O compound photocatalyst and application in treating organic dyes," *Journal of Hazardous Materials*, vol. 176, no. 1–3, pp. 807–813, 2010.

[5] P. Li, Z. Wei, T. Wu, Q. Peng, and Y. Li, "Au–ZnO hybrid nanopyramids and their photocatalytic properties," *Journal of the American Chemical Society*, vol. 133, no. 15, pp. 5660–5663, 2011.

[6] W. Wu, S. Zhang, X. Xiao et al., "Controllable synthesis, magnetic properties, and enhanced photocatalytic activity of spindlelike mesoporous α-Fe_2O_3/ZnO core–shell heterostructures," *ACS Applied Materials & Interfaces*, vol. 4, no. 7, pp. 3602–3609, 2012.

[7] R. Saravanan, S. Karthikeyan, V. Gupta, G. Sekaran, V. Narayanan, and A. Stephen, "Enhanced photocatalytic activity of ZnO/CuO nanocomposite for the degradation of textile dye on visible light illumination," *Materials Science and Engineering: C*, vol. 33, no. 1, pp. 91–98, 2013.

[8] B. Li and Y. Wang, "Facile synthesis and photocatalytic activity of ZnO–CuO nanocomposite," *Superlattices and Microstructures*, vol. 47, no. 5, pp. 615–623, 2010.

[9] A. Kargar, Y. Jing, S. J. Kim, C. T. Riley, X. Pan, and D. Wang, "ZnO/CuO heterojunction branched nanowires for photoelectrochemical hydrogen generation," *ACS Nano*, vol. 7, no. 12, pp. 11112–11120, 2013.

[10] Y. Zhang, S. Yuan, G. Day, X. Wang, X. Yang, and H.-C. Zhou, "Luminescent sensors based on metal-organic frameworks," *Coordination Chemistry Reviews*, vol. 354, pp. 28–45, 2018.

[11] H.-C. J. Zhou and S. Kitagawa, Eds., "Metal–organic frameworks (MOFs)," *Chemical Society Reviews*, vol. 43, no. 16, pp. 5415–5418, 2014.

[12] K. K. Gangu, S. Maddila, S. B. Mukkamala, and S. B. Jonnalagadda, "A review on contemporary metal–organic framework materials," *Inorganica Chimica Acta*, vol. 446, pp. 61–74, 2016.

[13] S. S.-Y. Chui, S. M.-F. Lo, J. P. H. Charmant, A. G. Orpen, and I. D. Williams, "A chemically functionalizable nanoporous material $[Cu_3(TMA)_2(H_2O)_3]n$," *Science*, vol. 283, no. 5405, pp. 1148–1150, 1999.

[14] S. L. Ho, I. C. Yoon, C. S. Cho, and H.-J. Choi, "A recyclable metal-organic framework MOF-199 catalyst in coupling and cyclization of β-bromo-α,β-unsaturated carboxylic acids with terminal alkynes leading to alkylidenefuranones," *Journal of Organometallic Chemistry*, vol. 791, pp. 13–17, 2015.

[15] Y. Jiang, X. Zhang, X. Dai et al., "Microwave-assisted synthesis of ultrafine Au nanoparticles immobilized on MOF-199 in high loading as efficient catalysts for a three-component coupling reaction," *Nano Research*, vol. 10, no. 3, pp. 876–889, 2017.

[16] E. Ghorbani-Kalhor, "A metal-organic framework nanocomposite made from functionalized magnetite nanoparticles and HKUST-1 (MOF-199) for preconcentration of Cd(II), Pb(II), and Ni(II)," *Microchimica Acta*, vol. 183, no. 9, pp. 2639–2647, 2016.

[17] M. Anbia, M. Faryadras, and A. Ghaffarinejad, "Synthesis and characterization of $Zn_3(BTC)_2$ nanoporous sorbent and its application for hydrogen storage at ambient temperature," *Journal of Applied Chemical Research*, vol. 9, no. 3, pp. 33–41, 2015.

[18] A. A. Tehrani, V. Safarifard, A. Morsali, G. Bruno, and H. A. Rudbari, "Ultrasound-assisted synthesis of metal–organic framework nanorods of Zn-HKUST-1 and their templating effects for facile fabrication of zinc oxide nanorods via solid-state transformation," *Inorganic Chemistry Communications*, vol. 59, pp. 41–45, 2015.

[19] L. Xu, E.-Y. Choi, and Y.-U. Kwon, "Ionothermal synthesis of a 3D Zn–BTC metal-organic framework with distorted tetranuclear $[Zn_4(\mu_4\text{-O})]$ subunits," *Inorganic Chemistry Communications*, vol. 11, no. 10, pp. 1190–1193, 2008.

[20] J. I. Feldblyum, M. Liu, D. W. Gidley, and A. J. Matzger, "Reconciling the discrepancies between crystallographic porosity and guest access as exemplified by Zn-HKUST-1," *Journal of the American Chemical Society*, vol. 133, no. 45, pp. 18257–18263, 2011.

[21] C. T. Pereira da Silva, B. N. Safadi, M. P. Moisés et al., "Synthesis of Zn-BTC metal organic framework assisted by a home microwave oven and their unusual morphologies," *Materials Letters*, vol. 182, pp. 231–234, 2016.

[22] H. Guo, T. Li, W. Chen et al., "General design of hollow porous $CoFe_2O_4$ nanocubes from metal–organic frameworks with extraordinary lithium storage," *Nanoscale*, vol. 6, pp. 15168–15174, 2014.

[23] S. Chen, M. Xue, Y. Li et al., "Porous $ZnCo_2O_4$ nanoparticles derived from a new mixed-metal organic framework for supercapacitors," *Inorganic Chemistry Frontiers*, vol. 2, pp. 177–183, 2015.

[24] H. D. Mai, K. Rafiq, and H. Yoo, "Nano metal-organic framework-derived inorganic hybrid nanomaterials: synthetic strategies and applications," *Chemistry–A European Journal*, vol. 23, pp. 5631–5651, 2017.

[25] X. Xu, K. Cao, Y. Wang, and L. Jiao, "3D hierarchical porous $ZnO/ZnCo_2O_4$ nanosheets as high-rate anode material for lithium-ion batteries," *Journal of Materials Chemistry A*, vol. 4, pp. 6042–6047, 2016.

[26] G. Huang, F. Zhang, L. Zhang, X. Du, J. Wang, and L. Wang, "Hierarchical $NiFe_2O_4/Fe_2O_3$ nanotubes derived from metal organic frameworks for superior lithium ion battery anodes," *Journal of Materials Chemistry A*, vol. 2, pp. 8048–8053, 2014.

[27] R. Wu, X. Qian, K. Zhou, J. Wei, J. Lou, and P. M. Ajayan, "Porous spinel $Zn_xCo_{3-x}O_4$ hollow polyhedra templated for high-rate lithium-ion batteries," *ACS Nano*, vol. 8, pp. 6297–6303, 2014.

[28] X. Lei, Y. Cao, Q. Chen, X. Ao, Y. Fang, and B. Liu, "ZIF-8 derived hollow CuO/ZnO material for study of enhanced photocatalytic performance," *Colloids and Surfaces A: Physicochemical and Engineering Aspects*, vol. 568, pp. 1–10, 2019.

[29] T. T. Minh, N. H. Phong, H. Van Duc, and D. Q. Khieu, "Microwave synthesis and voltammetric simultaneous determination of paracetamol and caffeine using an MOF-199-based electrode," *Journal of Materials Science*, vol. 53, no. 4, pp. 2453–2471, 2018.

[30] H. Wang, X. Yuan, Y. Wu et al., "Synthesis and applications of novel graphitic carbon nitride/metal-organic frameworks mesoporous photocatalyst for dyes removal," *Applied Catalysis B: Environmental*, vol. 174-175, pp. 445–454, 2015.

[31] W.-T. Xu, L. Ma, F. Ke et al., "Metal–organic frameworks MIL-88A hexagonal microrods as a new photocatalyst for efficient decolorization of methylene blue dye," *Dalton Transactions*, vol. 43, pp. 3792–3798, 2014.

[32] V. Stavila, J. Volponi, A. M. Katzenmeyer, M. C. Dixon, and M. D. Allendorf, "Kinetics and mechanism of metal–organic framework thin film growth: systematic investigation of HKUST-1 deposition on QCM electrodes," *Chemical Science*, vol. 3, pp. 1531–1540, 2012.

[33] L. H. Wee, M. R. Lohe, N. Janssens, S. Kaskel, and J. A. Martens, "Fine tuning of the metal–organic framework $Cu_3(BTC)_2$ HKUST-1 crystal size in the 100 nm to 5 micron range," *Journal of Materials Chemistry*, vol. 22, pp. 13742–13746, 2012.

[34] N. M. Mahmoodi and J. Abdi, "Nanoporous metal-organic framework (MOF-199): synthesis, characterization and photocatalytic degradation of basic blue 41," *Microchemical Journal*, vol. 144, pp. 436–442, 2019.

[35] T. V. N. Thi, C. L. Luu, T. C. Hoang et al., "Synthesis of MOF-199 and application to CO_2 adsorption," *Advances in Natural Sciences: Nanoscience and Nanotechnology*, vol. 4, no. 3, article 035016, 2013.

[36] X. Zhang, H. Li, X. Lv et al., "Facile synthesis of highly efficient amorphous Mn-MIL-100 catalysts: formation mechanism and structure changes during application in CO oxidation," *Chemistry - A European Journal*, vol. 24, no. 35, pp. 8822–8832, 2018.

[37] L. Cui, D. Zhao, Y. Yang, Y. Wang, and X. Zhang, "Synthesis of highly efficient α-Fe_2O_3 catalysts for CO oxidation derived from MIL-100(Fe)," *Journal of Solid State Chemistry*, vol. 247, pp. 168–172, 2017.

[38] Y. Yang, H. Dong, Y. Wang, C. He, Y. Wang, and X. Zhang, "Synthesis of octahedral like Cu-BTC derivatives derived from

MOF calcined under different atmosphere for application in CO oxidation," *Journal of Solid State Chemistry*, vol. 258, pp. 582–587, 2018.

[39] P. Sathishkumar, R. Sweena, J. J. Wu, and S. Anandan, "Synthesis of CuO-ZnO nanophotocatalyst for visible light assisted degradation of a textile dye in aqueous solution," *Chemical Engineering Journal*, vol. 171, no. 1, pp. 136–140, 2011.

[40] S. Pal, S. Maiti, U. N. Maiti, and K. K. Chattopadhyay, "Low temperature solution processed ZnO/CuO heterojunction photocatalyst for visible light induced photo-degradation of organic pollutants," *CrystEngComm*, vol. 17, no. 6, pp. 1464–1476, 2015.

[41] L. Xu, B. Wei, W. Liu, H. Zhang, C. Su, and J. Che, "Flower-like ZnO-Ag_2O composites: precipitation synthesis and photocatalytic activity," *Nanoscale Research Letters*, vol. 8, no. 1, p. 536, 2013.

[42] J. Tauc, "Optical properties and electronic structure of amorphous Ge and Si," *Materials Research Bulletin*, vol. 3, no. 1, pp. 37–46, 1968.

[43] K.-F. Lin, H.-M. Cheng, H.-C. Hsu, L.-J. Lin, and W.-F. Hsieh, "Band gap variation of size-controlled ZnO quantum dots synthesized by sol–gel method," *Chemical Physics Letters*, vol. 409, no. 4–6, pp. 208–211, 2005.

[44] Y. Xu and M. A. A. Schoonen, "The absolute energy positions of conduction and valence bands of selected semiconducting minerals," *American Mineralogist*, vol. 85, no. 3-4, pp. 543–556, 2000.

[45] Y. S. Chaudhary, A. Agrawal, R. Shrivastav, V. R. Satsangi, and S. Dass, "A study on the photoelectrochemical properties of copper oxide thin films," *International Journal of Hydrogen Energy*, vol. 29, no. 2, pp. 131–134, 2004.

[46] K. Santra, C. Sarkar, M. Mukherjee, and B. Ghosh, "Copper oxide thin films grown by plasma evaporation method," *Thin Solid Films*, vol. 213, no. 2, pp. 226–229, 1992.

[47] M. V. Lopez-Ramon, F. Stoeckli, C. Moreno-Castilla, and F. Carrasco-Marin, "On the characterization of acidic and basic surface sites on carbons by various techniques," *Carbon*, vol. 37, no. 8, pp. 1215–1221, 1999.

[48] B. Dhale, S. Mujawar, S. Bhattar, and P. Patil, "Chemical properties of n-ZnO/p-CuO heterojunctions for photovoltaic applications," *Der Chemica Sinica*, vol. 5, pp. 59–64, 2014.

[49] H. Seema, K. C. Kemp, V. Chandra, and K. S. Kim, "Graphene–SnO_2 composites for highly efficient photocatalytic degradation of methylene blue under sunlight," *Nanotechnology*, vol. 23, no. 35, article 355705, 2012.

[50] T. Shen, Z.-G. Zhao, Q. Yu, and H.-J. Xu, "Photosensitized reduction of benzil by heteroatom-containing anthracene dyes," *Journal of Photochemistry and Photobiology A: Chemistry*, vol. 47, no. 2, pp. 203–212, 1989.

[51] M. J. Islam, D. A. Reddy, J. Choi, and T. K. Kim, "Surface oxygen vacancy assisted electron transfer and shuttling for enhanced photocatalytic activity of a Z-scheme CeO_2–AgI nanocomposite," *RSC Advances*, vol. 6, no. 23, pp. 19341–19350, 2016.

[52] H. Fan, X. Zhao, J. Yang et al., "ZnO–graphene composite for photocatalytic degradation of methylene blue dye," *Catalysis Communications*, vol. 29, pp. 29–34, 2012.

[53] Y. Wang, R. Shi, J. Lin, and Y. Zhu, "Significant photocatalytic enhancement in methylene blue degradation of TiO_2 photocatalysts via graphene-like carbon in situ hybridization," *Applied Catalysis B: Environmental*, vol. 100, no. 1-2, pp. 179–183, 2010.

[54] P. Du, A. Bueno-Lopez, M. Verbaas et al., "The effect of surface OH-population on the photocatalytic activity of rare earth-doped P25-TiO_2 in methylene blue degradation," *Journal of Catalysis*, vol. 260, no. 1, pp. 75–80, 2008.

[55] A. Houas, H. Lachheb, M. Ksibi, E. Elaloui, C. Guillard, and J.-M. Herrmann, "Photocatalytic degradation pathway of methylene blue in water," *Applied Catalysis B: Environmental*, vol. 31, no. 2, pp. 145–157, 2001.

[56] F. Jiang, T. Yan, H. Chen, A. Sun, C. Xu, and X. Wang, "Ag-C_3N_4–CdS composite catalyst with high visible-light-driven catalytic activity and photostability for methylene blue degradation," *Applied Surface Science*, vol. 295, pp. 164–172, 2014.

[57] T.-J. Whang, M.-T. Hsieh, and H.-H. Chen, "Visible-light photocatalytic degradation of methylene blue with laser-induced Ag/ZnO nanoparticles," *Applied Surface Science*, vol. 258, no. 7, pp. 2796–2801, 2012.

[58] J.-Z. Kong, A.-D. Li, X.-Y. Li et al., "Photo-degradation of methylene blue using Ta-doped ZnO nanoparticle," *Journal of Solid State Chemistry*, vol. 183, no. 6, pp. 1359–1364, 2010.

[59] D. A. Quang, T. T. T. Toan, T. Q. Tung, T. T. Hoa, T. X. Mau, and D. Q. Khieu, "Synthesis of CeO_2/TiO_2 nanotubes and heterogeneous photocatalytic degradation of methylene blue," *Journal of Environmental Chemical Engineering*, vol. 6, no. 5, pp. 5999–6011, 2018.